

## Design and characterization of a nano-Newton resolution thrust stand

J. Soni and S. Roy

Citation: *Rev. Sci. Instrum.* **84**, 095103 (2013); doi: 10.1063/1.4819252

View online: <http://dx.doi.org/10.1063/1.4819252>

View Table of Contents: <http://rsi.aip.org/resource/1/RSINAK/v84/i9>

Published by the AIP Publishing LLC.

---

### Additional information on Rev. Sci. Instrum.

Journal Homepage: <http://rsi.aip.org>

Journal Information: [http://rsi.aip.org/about/about\\_the\\_journal](http://rsi.aip.org/about/about_the_journal)

Top downloads: [http://rsi.aip.org/features/most\\_downloaded](http://rsi.aip.org/features/most_downloaded)

Information for Authors: <http://rsi.aip.org/authors>

## ADVERTISEMENT

**physicstoday**

Comment on any  
*Physics Today* article.

Physics Today / Volume 63 / Issue 7 / July 2012  
Previous Article | Next Article

**Measured energy in Japan**  
David von Seggern  
(dovseg@seismo.unr.edu) University of Nevada  
July 2012, page 10  
DIGITAL OBJECT IDENTIFIER  
<http://dx.doi.org/10.1063/PT.3.1619>

The article by Thorne Lay and Hiroo Kanamori (PT 3.1619) is an excellent review of the energy released by the 2011 Tohoku earthquake. The authors estimate that the earthquake released approximately five times as much energy as the 1964 Chilean earthquake. This is a significant finding, especially since the 1964 Chilean earthquake had still more energy by a factor of about 3, or 15 times as much energy as the 1964 Chilean earthquake. The authors used the relation for seismic energy release rather than total strain energy release. I believe the authors underestimated the total strain energy release by a variable that depends on friction on the fault plane. Accounting for total strain energy release would increase the earthquake energy number by orders of magnitude.

Despite the catastrophic damage potential of nuclear bombs, the forces of nature occasionally unleash much larger energy releases. Although the nuclear bombs are under our control, earthquakes, volcanic eruptions, and extreme weather events are not. However, by judicious preparation and avoidance measures, humans can significantly diminish the damage of natural events.

This article does not have any references.

**Comment on this article**  
By the act of hitting a ball with a bat, one calculates the force energy to deliver the ball to its new location, but one must also take into account that the ball extended its energy to the entire team, which became struck by the ball as its momentum ceased and passed energy to the entire team. Therefore the parameters of the damage extend into the future when the received energy to that pushed upon, later becomes released in a new event. Perhaps calculations of one added that in, while another's calculations did not. E.M.C.  
Written by Edgar Mocarvill, 14 July 2012 19:59

## Design and characterization of a nano-Newton resolution thrust stand

J. Soni and S. Roy<sup>a)</sup>

Applied Physics Research Group, University of Florida, Gainesville, Florida 32611, USA

(Received 12 July 2013; accepted 12 August 2013; published online 3 September 2013)

The paper describes the design, calibration, and characterization of a thrust stand capable of nano-Newton resolution. A low uncertainty calibration method is proposed and demonstrated. A passive eddy current based damper, which is non-contact and vacuum compatible, is employed. Signal analysis techniques are used to perform noise characterization, and potential sources are identified. Calibrated system noise floor suggests thrust measurement resolution of the order of 10 nN is feasible under laboratory conditions. Force measurement from this balance for a standard macroscale dielectric barrier discharge (DBD) plasma actuator is benchmarked with a commercial precision balance of 9.8  $\mu\text{N}$  resolution and is found to be in good agreement. Published results of a microscale DBD plasma actuator force measurement and low pressure characterization of conventional plasma actuators are presented for completeness. © 2013 AIP Publishing LLC. [<http://dx.doi.org/10.1063/1.4819252>]

### I. INTRODUCTION AND MOTIVATION

The advent of nanosatellites has given rise to a new challenge in the field of space propulsion. These satellites, typically weighing between 1 and 10 kg, require very minute forces for executing maneuvers for station keeping, orbital corrections, and attitude control. These forces are often of the order of a few micronewtons or less. Although the design for thrusters capable of delivering these forces has been around for some time,<sup>1</sup> the need for a simple, low cost measurement method exists that resolves these sub-micro-Newton forces accurately and reliably.

Here, we report the design and characterization of a thrust stand based on the principle of a torsion balance. The device is essentially a torsion spring, which undergoes angular deflections under the action of a torque. This angular deflection, generated by an unknown force acting at a known distance, can be measured as linear displacement of the balance arm at a known distance from the pivot. The device was first conceived by Charles Coulomb to measure the electrostatic force leading to the discovery of the Coulomb Law,<sup>2</sup> and later by Henry Cavendish to measure the gravitational force between two masses.<sup>3</sup>

Jamison *et al.*,<sup>4</sup> Ziemer,<sup>5</sup> Gamero-Castaño *et al.*,<sup>6</sup> Gamero-Castaño,<sup>7</sup> and Yang *et al.*<sup>8</sup> have all built thrust stands with the same fundamental working principle, albeit with different methods of calibration, damping techniques, and displacement measurement. Table I summarizes the details and the steady-state force resolution achieved by each of these.

Note that the orifice thruster used by Jamison *et al.*<sup>4</sup> was calibrated using DSMC techniques, and the lowest thrust measured was 88.8 nN. Actual steady state thrust measured by Ziemer<sup>5</sup> was 1  $\mu\text{N}$  using a FEEP thruster. The lowest thrust measured by Gamero-Castaño *et al.*<sup>6</sup> was 0.11  $\mu\text{N}$  using an electrospray source, and 7.89  $\mu\text{N}$  using a colloid thruster by Gamero-Castaño.<sup>7</sup> Although Ref. 6 has the same resolution as the design presented herein, current design uses a passive damper and a better calibration method. Yang *et al.*<sup>8</sup> used a

pendulum stage suspended from 502  $\mu\text{m}$  titanium fiber which acts as the torsion spring. No damping other than that provided by surrounding air was employed, and the thrust stand was calibrated by measuring the moment of inertia of the setup and oscillation frequency. The resolution for steady-state thrust is mentioned to be 0.09  $\mu\text{N}$ . In comparison, the lowest thrust measured using the Applied Physics Research Group micro-Newton thrust stand (hereafter called APRG  $\mu\text{NTS}$ ) is 1.3  $\mu\text{N}$  with an uncertainty of  $\pm 20\%$ .

### II. THE APRG $\mu\text{NTS}$

The APRG  $\mu\text{NTS}$  is essentially a torsion balance and was conceived as part of a larger experiment to develop a plasma based micro-thruster called the Free Molecular Electro Jet (FMEJ)<sup>9</sup> capable of delivering sub-micronewton level thrust for nanosatellites. The thrust stand aims to resolve forces smaller than 1 micronewton, preferably down to several nano-Newtons ( $\sim 10$  nN). Since the torsion balance is a proportional balance, it needs *a priori* calibration before forces can be measured reliably and with known certainty.

Figure 1 schematic shows a 3D rendering of the APRG  $\mu\text{NTS}$ . The two flexure pivots at the vertical ends of the cross-beam form the torsion spring providing the restoring torque. The cross-beam is laterally unsymmetrical to optimize the sensitivity within the space constraints (the entire system must fit inside a vacuum chamber sized 10"  $\times$  10"  $\times$  22" with enough clearance).

The copper block, suspended at the short end of the cross-beam, acts as a counterweight and balances the unsymmetrical beam. A pair of aluminum disc electrodes provides a known force or controlled displacement for calibration. An optical linear displacement sensor (Philtec Model D-100) measures the displacement of the balance arm at a distance to calculate the angular deflection.

### III. TORSION BALANCE DYNAMICS

The  $\mu\text{NTS}$  is essentially a torsion pendulum. The statics and dynamics of an *undamped* torsion balance can be

<sup>a)</sup>Email: roy@ufl.edu

TABLE I. Review of thrust stands with sub-micro-Newton level resolution.

Team	Calibration source	Damping mechanism	Displacement measurement	Resolution ( $\mu\text{N}$ )	Lowest thrust measured ( $\mu\text{N}$ )
Jamison <i>et al.</i> <sup>4</sup>	Orifice thruster	Viscous oil bath	LVDT	<1	0.088 ( $\pm 2\%$ –16%)
Ziemer <sup>5</sup>	Impact pendulum	Damping coil	LVDT	<1	1.0 ( $\pm 20\%$ )
Gamero-Castaño <i>et al.</i> <sup>6</sup>	Electrostatic	Electrostatic	Fiber optic LDS	0.01	0.11
Gamero-Castaño <sup>7</sup>	Electrostatic	Electrostatic	Fiber optic LDS	0.03	7.89
Yang <i>et al.</i> <sup>8</sup>	Free oscillations	Air damping	Autocollimator	0.09	Not mentioned
Soni and Roy <sup>12</sup>	Log decrement	Eddy current	Fiber optic LDS	0.01	1.3 ( $\pm 20\%$ )

completely characterized by two parameters: the torsion spring constant  $k_\theta$  and the moment of inertia (MI) of the system  $I_\theta$ , which govern the natural frequency of the system as

$$\omega_n = \sqrt{\frac{k_\theta}{I_\theta}}. \quad (1)$$

However, for practical reasons, damping is desired to bring the system to a steady state, facilitating quick readings. For such a damped system, the equation of motion is

$$\ddot{\theta} + 2\zeta\omega_n\dot{\theta} + \omega_n^2\theta = \frac{f(t)l_T}{I_\theta}, \quad (2)$$

where  $\theta(t)$  is the instantaneous deflection angle,  $\zeta$  is the damping coefficient,  $f(t)$  is the time dependent force, and  $l_T$  is the distance from the pivot at which the force forms a torque (moment arm).

For a constant force  $f(t) = F$ , Ziemer<sup>5</sup> gives the solution to Eq. (2) as

$$\theta(t) = \frac{Fl_T}{I_\theta\omega_n^2} \left[ 1 - \exp(-\zeta\omega_n t) \times \left( \frac{\zeta}{\sqrt{1-\zeta^2}} \sin(\sqrt{1-\zeta^2}\omega_n t) + \sin(\sqrt{1-\zeta^2}\omega_n t) \right) \right], \quad (3)$$

the steady state solution to which can be written (using small angular displacement  $\theta = \frac{x}{l_s} \cdot \frac{180}{\pi}$ ) as

$$\theta(t \rightarrow \infty) = \frac{F \cdot l_T}{k_\theta} \Rightarrow F = \frac{\theta(\infty) \cdot k_\theta}{l_T} \Rightarrow F = \frac{k_\theta x}{l_T l_s} \frac{180}{\pi}. \quad (4)$$

Hence, knowing the steady state linear displacement  $x$ , the spring constant  $k_\theta$ , the moment arm length  $l_T$ , and the sensor distance  $l_s$ , the unknown force  $F$  can be readily calculated. For a given resolution of linear displacement  $x$ , the force resolution can be maximized either by increasing the

moment length and the sensor distance, or by using torsion springs with a lower spring constant. The moment length and the sensor distance are constrained by the operating envelop of the stand, whilst there is a tradeoff between lower spring constants and the axial and radial load bearing capacity of the springs. As a conservative measure, the current springs are chosen to have a load bearing capacity of 98 lbs, more than what the thrust stand would be required to withstand.

For the current design, both the sensor and the calibration electrodes are located at a distance of 28.5 cm from the pivot axis ( $l_s = l_T = l$ ). The torsion springs, procured from Riverhawk Company, have a rated spring constant of 0.0016 N-m/deg each, with an accuracy of  $\pm 10\%$ . In the given configuration, the two torsion springs act in parallel (due to identical displacements), hence the total spring constant is just a numerical sum giving a mean total spring constant for the system of around 0.0032 N-m/deg. Having these two parameters fixed by design, the resolution of the stand is limited only by the resolution with which the linear displacement  $x$  can be measured, and the accuracy with which the system can be calibrated.

#### IV. DAMPING MECHANISM

Damping a dynamical system is of critical importance to minimize noise and reduce the time required to reach a stable deflection of the balance arm. In the absence of damping, the balance arm vibrates for a significant duration (Fig. 2(a)), with ambient air providing only minimal damping, apart from structural/thermal dissipation at the torsion springs. To make the system damp more rapidly, a magnetic damper was introduced based on eddy current damping. A similar concept for damping of torsion balance oscillations was demonstrated by Polzin *et al.*<sup>10</sup> Their thrust stand, however, had an ultimate resolution of 50  $\mu\text{N}$ , 3 orders of magnitude lower than

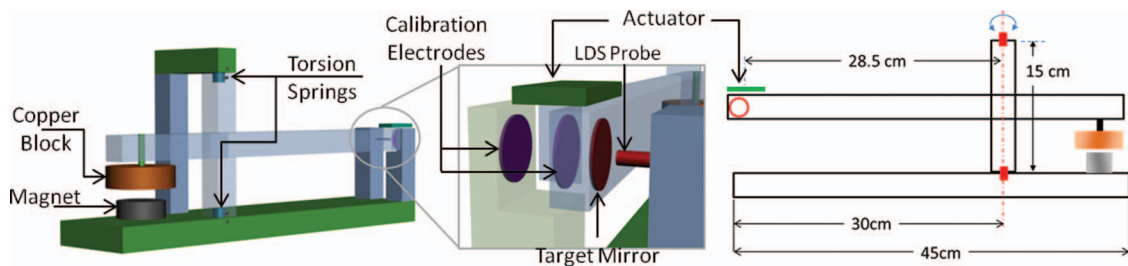


FIG. 1. Details of the APRG uNTS.

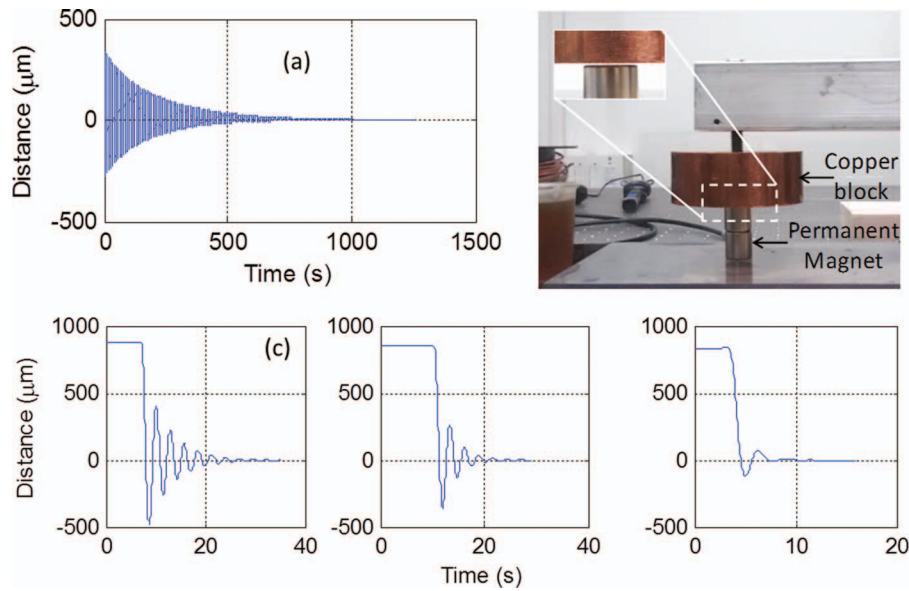


FIG. 2. (a) Undamped oscillations, (b) magnetic damper, and (c) damped oscillations with increasing damping.

that aimed by the  $\mu$ NTS. For the  $\mu$ NTS damper, a cylindrical copper block ( $2\frac{1}{2}$ " dia.  $\times$  1" height) of high conductivity was mounted on the balance arm, with a neodymium permanent magnet ( $1/2$ " dia.  $\times$  1" height,  $B_{surface} = 6619$  Gauss<sup>11</sup>) placed under it in close proximity ( $O(\text{mm})$ , Fig. 2(b)). As the beam oscillates, the relative motion of the copper block and the magnet induces eddy currents in the block, which generate their own magnetic field counter to the applied magnetic field. The applied and induced magnetic fields interact to produce a retarding force proportional to the relative motion, essentially providing damping. The amount of damping can be controlled by controlling the gap between the copper block and the permanent magnet (0.5–3 mm), and close-to-critical damping can be achieved (Fig. 2(c)). Magnetic damping has inherent advantages of being a non-contact and vacuum compatible (as opposed to a viscous damper). It also does not require a power source and an active closed loop control (as opposed to an electrostatic/electromagnetic damper). This setup provides similar damping characteristics as a viscous damper using Lucas Heavy Duty Oil Stabilizer with a specific gravity of 0.895 and viscosity of  $1.1 \times 10^{-4}$  m<sup>2</sup>/s.

## V. CALIBRATION

As reported in Table I, several methods of calibration have been reported in literature. Most of these rely on a device which can produce an accurately known force against which the system is calibrated, with exceptions like the impact pendulum used by Ziemer<sup>5</sup> which relies on applying a known impulse instead of a steady-state force to back out the system dynamics. The orifice thruster, used by Jamison *et al.*,<sup>4</sup> itself is calibrated using Monte Carlo methods, which introduce a certain amount of uncertainty ( $\pm 12.6\%$ ) in the exact force that the thruster delivers. The electrostatic force calibration implemented by Gamero-Castaño *et al.*<sup>6</sup> and Gamero-Castaño<sup>7</sup> has its own disadvantages. The following error analysis shows

that this (electrostatic) method inherently introduces multiple sources of error, necessitating a better calibration method.

The force between two identical parallel plate electrodes separated by a distance  $L$  and having area  $A$  is given by

$$F = \frac{1}{2} \epsilon \left( \frac{V}{L} \right)^2 A. \quad (5)$$

Combining Eqs. (4) and (5), the calibration constant  $k_\theta$  can be written as

$$k_\theta = \frac{\epsilon}{2} \cdot V^2 \cdot \frac{1}{L^2} \cdot A \cdot l^2 \cdot \frac{1}{x}. \quad (6)$$

Applying error propagation analysis to this equation yields the following equation for relative uncertainty in  $k_\theta$ ,

$$\frac{\partial k_\theta}{k_\theta} = \sqrt{\left( \frac{2dV}{V} \right)^2 + \left( \frac{2dL}{L} \right)^2 + \left( \frac{dA}{A} \right)^2 + \left( \frac{2dl}{l} \right)^2 + \left( \frac{dx}{x} \right)^2}. \quad (7)$$

As can be seen, there are five sources of error in the above calibration method, some of which can be controlled more precisely than others. The applied voltage  $V$ , electrode area  $A$ , and the moment length  $l$  can be controlled to a fair degree of accuracy. However, the electrode gap  $L$  (typically 1 mm), and the sensor resolution  $dx$  (5 nm as per manufacturer specifications at <http://www.philtec.com>, LDS Model D100) present the biggest challenge in controlling the spread of the calibration data. Equation (7) suggests that a 10% error in  $L$  alone leads to a 20% error in  $k_\theta$ . Accounting for errors from the other sources would increase this figure further.

To overcome this limitation, the system was calibrated using three different approaches, and the uncertainty and error sources in these methods were analyzed to choose the optimal method. The first method entailed observing the natural frequency of the undamped system to calculate the spring



constant using Eq. (1), which is reformulated as

$$k_\theta = \omega_n^2 \cdot I_\theta. \quad (8)$$

The moment of inertia (MI)  $I_\theta$  of the system is computed by superposition of the MIs of the component shapes and parallel axis theorem. This gives an estimate of  $I_\theta = 0.0385 \text{ kg}\cdot\text{m}^2$ . The natural frequency for the undamped system is observed to be 2.240 rad/s from the time-series of Figure 2(a). These values, in conjunction with Eq. (8), give an estimate for  $k_\theta$  of around 0.0034 N-m/deg, close to the stipulated value of 0.0032 (two springs in parallel, each with  $k_\theta = 0.0016 \text{ N-m/deg}$ ) and within the 10% error margin quoted by the manufacturer. Note that this value of  $k_\theta$  is only an approximation of the actual value to a certain error, since the system is not really undamped, as the air around the system provides a small but finite amount of damping. Therefore, a more accurate log-decrement method is used next to determine exactly how much damping the air provides and to compute a more precise estimate of  $k_\theta$ .

The log decrement method<sup>12</sup> backs out the damping ratio of the system based on successive peaks of damped oscillations, which, in conjunction with the observed damped frequency, provides an estimate of the spring constant,  $k_\theta$ . For  $n$  cycles of a damped oscillation, the logarithmic decrement  $\delta$  is defined as

$$\delta = \frac{1}{n} \ln \frac{x_0}{x_n}, \quad (9)$$

where  $x_0$  and  $x_n$  are the amplitudes of the first and  $n$ th peaks, respectively. The damping ratio  $\zeta$  is then found using the relation

$$\zeta = \frac{1}{\sqrt{1 + \left(\frac{2\pi}{\delta}\right)^2}}. \quad (10)$$

From the observed damped frequency  $\omega_d$  and the damping ratio, the natural frequency  $\omega_n$  can be estimated as

$$\omega_n = \frac{\omega_d}{\sqrt{1 - \zeta^2}}. \quad (11)$$

Finally, the spring constant then can be estimated from Eq. (8).

Applying this method to the data extracted from Fig. 2(a), we get an average value of  $k_\theta = 0.003379 \text{ N-m/deg}$  based on several values of  $n$ , demonstrating that neglecting air damping results in a nominal error of approximately 0.7%. The damping ratio in this case is found to be around 0.0028, justifying the undamped assumption.

The same analysis is applied to the system when it is damped using the magnetic damper. Since this is the configuration in which the setup will be used for future force measurement, a comprehensive set of calibration reading are taken at varying displacements, to ensure linearity of the spring constant over the desired range of displacement. Increasing displacements are produced by increasing the electrostatic force exerted by the parallel electrodes using higher voltage differentials, and the system is set to oscillate by turning off the voltage drop, and hence the force. As evident in Fig. 3, calibration values from both the electrostatic force and log

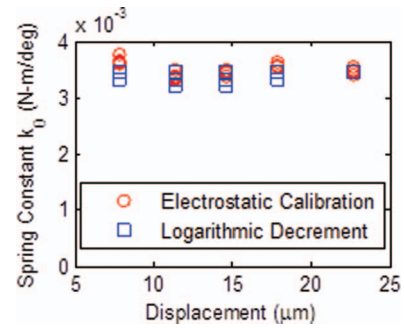


FIG. 3. Comparison between electrostatic force calibration and log decrement method.

decrement method are seen to converge around a value of 0.00345 N-m/deg, with a standard deviation of  $\sim 0.07\%$ . The spread in the data at lower displacements has to do with the fact the LDS signal-to-noise ratio decreases at lower displacement, leading to higher uncertainty in the results. Moreover, a slightly higher value than the nominal 0.0032 N-m/deg is to be expected, since the axial and radial loadings that the springs are under alter the spring constant slightly. This was further confirmed by a Riverhawk technical representative.

The log-decrement method offers the unique advantage that it is free from errors in the *source* used to generate the displacement and depends only on the response of the system itself. This greatly reduces the uncertainties associated with calibration process, with the only sources of error being the lower limit on the sensor resolution (which determines the uncertainty in  $\omega_n$ ), and the accuracy with which the MI of the system can be calculated. The uncertainty propagation relation for Eq. (8) would be

$$\frac{\partial k_\theta}{k_\theta} = \sqrt{\left(\frac{2d\omega_n}{\omega_n}\right)^2 + \left(\frac{dI_\theta}{I_\theta}\right)^2}. \quad (12)$$

The MI  $I_\theta$  can be measured to a high degree of certainty using a precision weighing scale and Vernier calipers. A simple uncertainty analysis suggests a good conservative estimate for  $dI_\theta$  would be 5%. The relative uncertainty estimate for  $\omega_n$  is not so straightforward since it depends on the way the errors in  $x_0$  and  $x_n$  propagate through Eqs. (9)–(11). The mathematical form of these equations results in an estimate which depends on the actual values of  $\delta$ ,  $\zeta$ , and  $\omega_n$ . Reasonable estimations based on typical values ( $\delta \sim 0.8$ ,  $\zeta \sim 0.14$ )

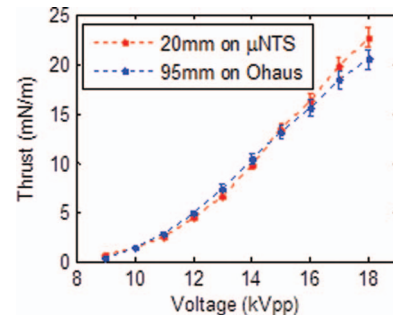


FIG. 4. Comparison of force measurement from commercial precision balance and  $\mu\text{NTS}$ .

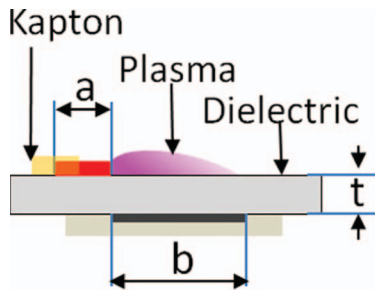


FIG. 5. Schematic of a plasma actuator, along with actuator details for macro and micro actuators.

suggest a 10% spread in  $\omega_n$ , which translates into a 20.6% error for  $k_\theta$ . Figure 3 suggests that the statistical scatter in  $k_\theta$  is also of the same order (20%).

To check how the  $\mu$ NTS compares against a commercial balance, a dielectric barrier discharge (DBD) plasma actuator was designed and tested on both the  $\mu$ NTS, and a commercial precision balance (Ohaus Adventurer Pro<sup>TM</sup> AC313C, 1 mg resolution). The actuator consisted of 1.5 mm thick acrylic with 5 mm wide powered electrode and a 20 mm wide ground. The upstream edge of the powered electrode was covered to prevent reverse discharge, and the ground electrode was covered with several layers of electrical tape. The actuator mounted on the commercial precision balance was 95 mm long (to produce enough force to assure a high signal-to-noise ratio), whereas the actuator mounted on the  $\mu$ NTS was 20 mm in length due to space and displacement constraints on the  $\mu$ NTS. Figure 4 suggests that the force per length results for the two actuators, as measured using the commercial balance and the APRG  $\mu$ NTS, seem to agree well. We see that direct force measurement from the  $\mu$ NTS start diverging at higher voltage (above 15 kVpp). This might have to do with the different downstream plate lengths of the two actuators, being shorter in case of the 20 mm actuator. Dürcher and Roy<sup>13</sup> have demonstrated that indeed a shorter downstream plate length leads to a higher force (by upto 20%) due to decreased drag loss along the plate surface. Although minor dimensional differences resulting from hand-fabrication of the actuators, and surface charge retention or

TABLE II. Details of the actuator geometries and operating parameters.

Setup	Dielectric	a (mm)	b (mm)	t (mm)	L (mm)	V (kVpp)	f (kHz)
Macro	Acrylic	5	20	1.5	20, 95	9–18	14
Micro	Polyamide	0.01–0.5	0.01–1.0	0.01	1.0	3–6.5	1

surface contamination could also be responsible for the observed deviation. Table II in conjunction with Figure 5 provides the details of the actuator geometries and operating parameters tested on the  $\mu$ NTS ( $a$  = powered electrode width,  $b$  = ground electrode width,  $t$  = dielectric thickness,  $L$  = actuator length,  $V$  = applied voltage, and  $f$  = applied frequency).

## VI. MEASUREMENT NOISE CHARACTERIZATION

The targeted resolution of the thrust stand renders it susceptible to a myriad of external and internal noise sources. The external sources include any external mechanical disturbance transmitted to the force balance by seismic or pressure disturbances. Clinton and Heaton<sup>14</sup> suggest the earth surface has a seismic background noise in the 0.01–10 Hz range, rendering any sensitive pendulum susceptible to seismic noise in this spectral range. To alleviate these disturbances, the thrust stand is housed inside a transparent isolation chamber to prevent from air drafts, and stationed on top of a heavy optical bench to emolliate seismic disturbances. Internal sources primarily include electrical noise in the LDS optical amplifier and electronics.

To characterize the internal  $\mu$ NTS noise, the signal from the linear displacement sensor pointed to a stationary target (a polished aluminum surface) is monitored over several different durations to identify and characterize any noise patterns. The arrangement was optically shielded from stray light to limit the noise to purely internal electrical sources. Figure 6 shows the sensor output over several different time scales. The plot of displacement over 8 hours (Fig. 6(a)) shows that the sensor reading drifts by upto 1.5  $\mu$ m over this duration, which corresponds to a force of about 3.6  $\mu$ N. Subtracting a linear fit of the drift from the signal over a 30-min period (Fig. 6(b)),

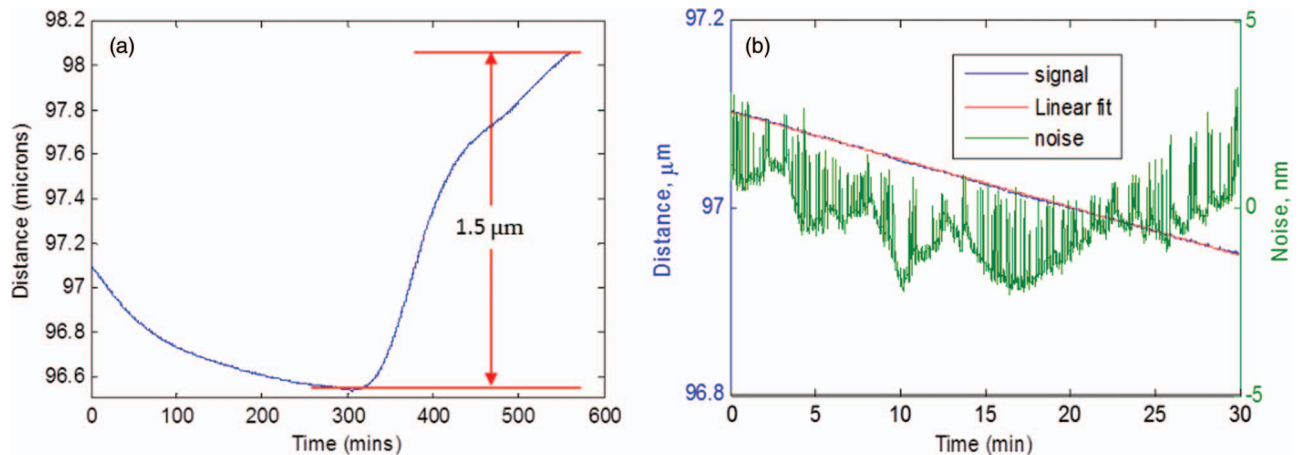


FIG. 6. (a) Sensor drift over a period of 8 h and (b) 30-min snapshot of the drift/noise profile.

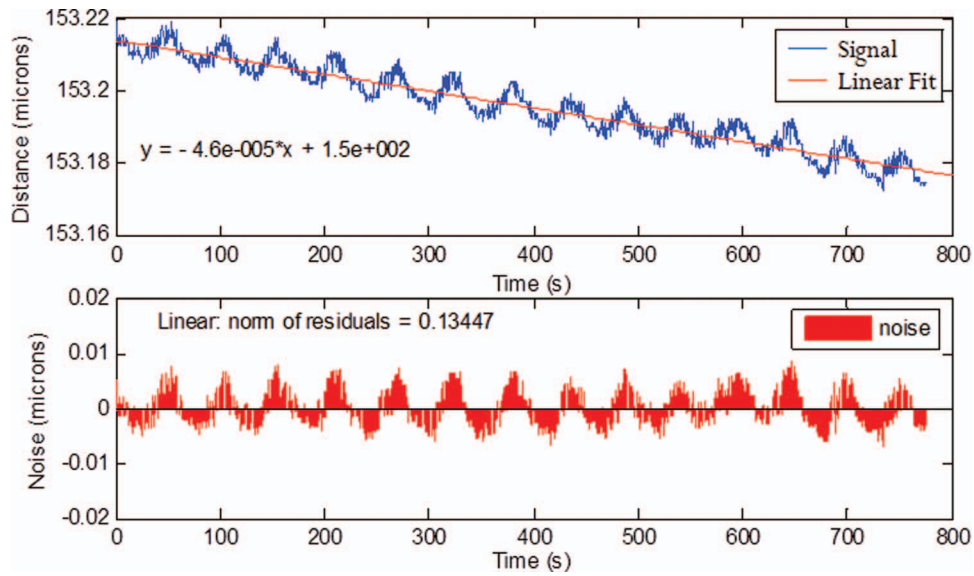


FIG. 7. Nature of the drift/noise (top) and residual around a linear fit showing periodic component (bottom).

the electrical noise of the displacement sensor is seen to be of the order of 5 nm, which corresponds to a force of about  $0.012 \mu\text{N}$ .

The drift is found to be extremely linear over short timescales (Fig. 6(b)), with  $R^2$  values of the linear fits approaching 0.99. This simplifies the task of drift correction since a typical force measurement lasts only a few minutes. Thermal expansion of the aluminum target resulting from ambient temperature fluctuations was identified as one possible cause. Hand calculations considering the size and coefficient of thermal expansion of the target, over the measured range of temperature fluctuations, further support this hypothesis.

To characterize the external noise, the sensor was integrated with the thrust stand, and readings taken without any force producing device mounted on the stand. Figure 7 (top) shows a 12 min plot of the sensor. The trend suggests a periodic noise superimposed on the linear drift. Residual of the original signal around a linear fit (Fig. 7, bottom) reveals a highly sinusoidal noise profile.

Autocorrelation analysis of the original signal (Fig. 8, top) produces a weak delta function coupled with superimposed sinusoidal noise, which is in agreement with the observed noise profile. Fast Fourier Transform of the autocorrelation function (Fig. 8, bottom) suggests a major peak at 0.01864 Hz, and two minor peaks at 0.01678 Hz and 0.001243 Hz.

Figure 9 shows the drift-subtracted noise from Fig. 7, and the single-sided frequency-amplitude spectrum of this noise profile obtained using FFT. This plot confirms the frequency peak at 0.01864 Hz, along with some minor peaks in the same vicinity as the FFT of the autocorrelation function. This frequency is several orders of magnitude lower than the 60 Hz mains noise that is a possible suspect. This is due to the fact that the sampling frequency for this time series (2.5 Hz) is 24 times less than the signal frequency, which leads to folding/aliasing. Using the concept of Nyquist frequency and knowing the apparent frequency from the FFT,

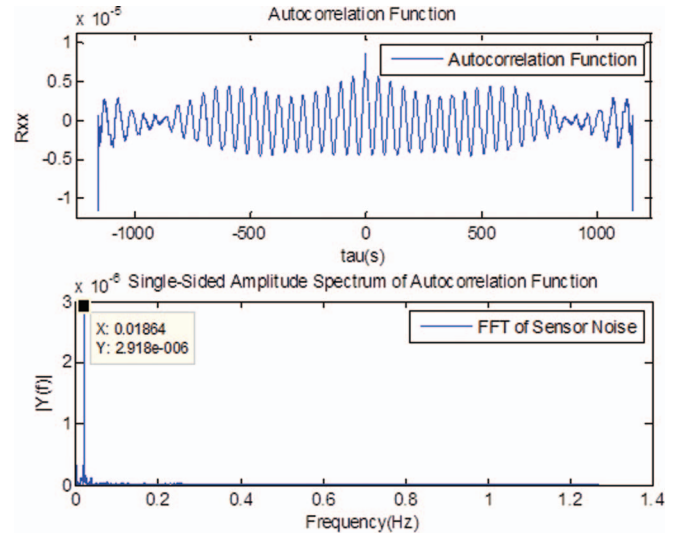


FIG. 8. Autocorrelation of sensor noise profile (top) and FFT of the autocorrelation function (bottom).

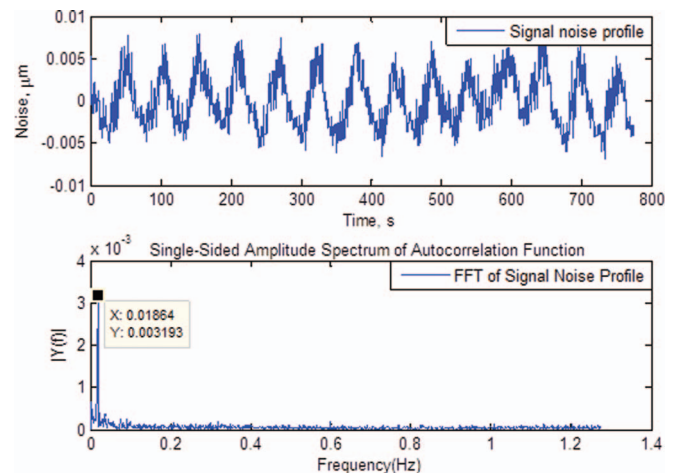


FIG. 9. Drift-subtracted sensor noise (top) and fast Fourier transform of this noise (bottom).

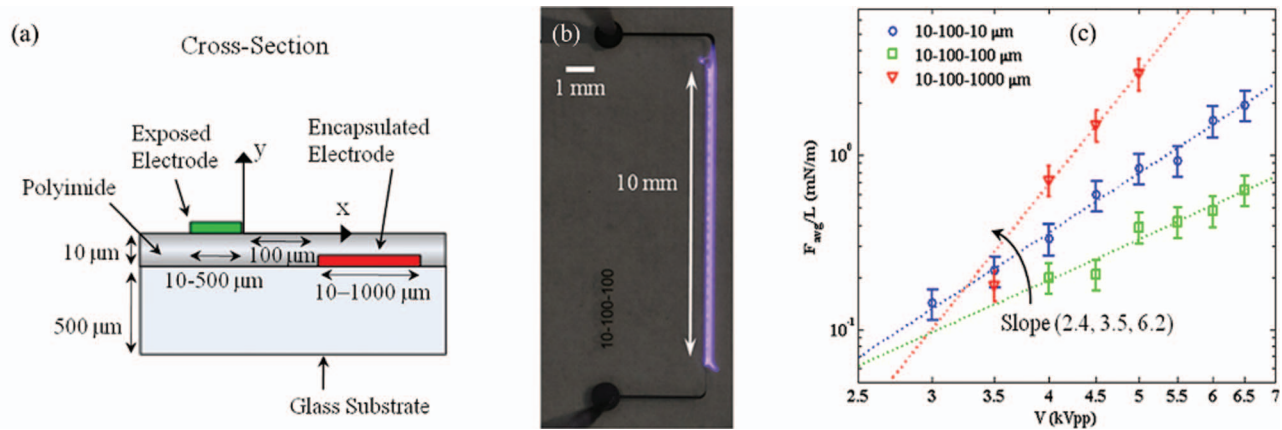


FIG. 10. (a) Schematic of a microactuator, (b) a powered device, and (c) force data from the  $\mu$ NTS. Reprinted with permission from J. Zito, R. Durscher, J. Soni, S. Roy, and D. Arnold, *Appl. Phys. Lett.* **100**, 193502 (2012). Copyright 2012 American Institute of Physics.

the frequency folding diagram is used to identify the actual frequency.<sup>15</sup> Results suggest 60.3 Hz as one of the possible source frequencies, which is within 0.03% of the mains frequency. Philtec representative later revealed the noise maybe due to stray light from fluorescent lighting, which is known to flicker at line frequency (60 Hz) or its second harmonic (120 Hz). A noise-corrected version of the sensor seemed to alleviate this problem.

## VII. FORCE VALIDATION AT MACRO AND MICRO SCALES

The  $\mu$ NTS has been used for measurement and characterization of force from DBD actuators of varying sizes, configurations, and at varying operating conditions. Zito *et al.*<sup>16</sup> have used the  $\mu$ NTS for measuring force from  $\mu$ m scale DBD actuators (Fig. 10). The actuators were made using photolithography techniques and have characteristic dimensions (dielectric thickness, electrode widths, and separation) of the order of  $\mu$ m. Scaling laws based on performance trends of macroactuators suggested such actuators should produce forces of the order of micronewtons. The  $\mu$ NTS was able to successfully resolve these forces as evident in Figure 10.

Soni and Roy<sup>17</sup> have used the  $\mu$ NTS to study low pressure performance of conventional (macroscale) DBD actuators. The thrust stand was able to function reliably *vis-à-vis* displacement measurements and damping when tested at pressures down to 20 Torr. The force trends were found to be in agreement with those based on low pressure force measurement from a commercial precision balance (Ohaus Adventurer Pro™ AV313C, resolution 1 mg), further confirming its reliability under a wide range of operating conditions. Figure 11 presents these results.

## VIII. CONCLUSIONS

The design and characterization of the torsional balance capable of nano-Newton level resolution was presented. The logarithmic decrement method was used for calibrating the stand. This method reduced the number of error sources and hence improved the calibration error margins compared to some previously reported methods. Importantly, a mechanism for damping the thrust stand oscillations, based on eddy current principles and using a permanent magnet and a copper block, was also demonstrated. This was a non-contact, fully vacuum compatible, and passive damper that did not require power or closed loop control. The damping ratio was easily

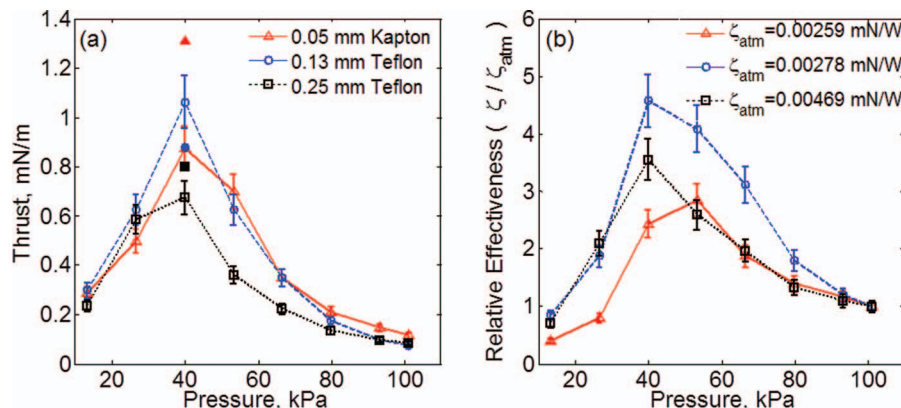


FIG. 11. Low pressure trends for DBD actuators obtained using the  $\mu$ NTS. (a) Thrust and (b) relative effectiveness. Reprinted with permission from J. Soni and S. Roy, *Appl. Phys. Lett.* **102**, 112908 (2013). Copyright 2013 American Institute of Physics.



controlled by adjusting the gap between a permanent magnet and a copper block, and a wide range of damping ratios was achieved. The thrust stand calibration was checked against a commercial precision balance and was found to be in good agreement. Both internal and external noise sources were studied and characterized. Internal noises (electrical) were found to be of the order of 5 nN (which correspond to  $\sim 10$  nN). External mechanical noises were significantly damped out by mounting the thrust stand inside an isolation chamber mounted on a heavy optical bench (Melles Griot Model OTN013). External stray optical noise was successfully identified as the cause of a sinusoidal noise component using signal analysis techniques, and a noise-corrected version of the sensor was introduced to further improve the thrust stand resolution. Previous validation of the thrust stand for measurement of  $\mu\text{m}$  sized actuators and measurements of macroscale actuators at lower than atmospheric pressures were also reported for completeness. These results affirm the reliability of the thrust stand over a wider range of operating parameters, including pressure.

<sup>1</sup>J. Mueller, "Thruster options for microspacecraft: A review and evaluation of state-of-the-art and emerging technologies," in *Micropropulsion for Small Spacecraft: Progress in Astronautics and Aeronautics, Vol. 187*, edited by M. Micci and A. Ketsdever (AIAA, Reston, VA, 2000), pp. 27–120.

<sup>2</sup>C. Coulomb, *Histoire de l'Académie Royale des Sciences* (Académie royale des sciences (France), Paris, 1785), pp. 569–577.

<sup>3</sup>H. Cavendish, "Experiments to determine the density of the earth," *Phil. Trans. R. Soc. Lond.* **88**, 469–526 (1798).

<sup>4</sup>A. Jamison, A. Ketsdever, and E. Muntz, "Accurate measurement of nano-Newton thrust for micropropulsion system characterization," *27th Inter-*

*national Electric Propulsion Conference, IEPC-01-236*, Pasadena, CA, 2001.

<sup>5</sup>J. Ziemer, "Performance measurements using a sub-micronewton resolution thrust stand," *27th International Electric Propulsion Conference, IEPC-01-238*, Pasadena, CA, 2001.

<sup>6</sup>M. Gamero-Castano, V. Hruby and M. Martinez-Sanchez, "A torsional balance that resolves sub-micro-Newton forces," *27th International Electric Propulsion Conference, IEPC-01-235*, Pasadena, CA, 2001.

<sup>7</sup>M. Gamero-Castaño, "A torsional balance for the characterization of microNewton thrusters," *Rev. Sci. Instrum.* **74**(10), 4509–4514 (2003).

<sup>8</sup>Y.-X. Yang, L.-C. Tu, S.-Q. Yang, and J. Luo, "A torsion balance for impulse and thrust measurements of micro-Newton thrusters," *Rev. Sci. Instrum.* **83**, 015105 (2012).

<sup>9</sup>S. Roy, "Method and apparatus for small satellite propulsion," UF Patent Application Patent 61/304,915, WO/2011/103194A2, 25 August 2011.

<sup>10</sup>K. Polzin, T. Markusic, B. Stanojev, A. DeHoyos, and B. Spaun, "Thrust stand for electric propulsion performance evaluation," *Rev. Sci. Instrum.* **77**, 105108 (2006).

<sup>11</sup>See <http://www.kjmagnetics.com> for magnet specifications.

<sup>12</sup>J. Soni and S. Roy, "Design of a microNewton thrust stand for low pressure characterization of DBD actuators," in *51st AIAA Aerospace Sciences Meeting*, Grapevine, TX, AIAA Paper 2013-0755, 2013.

<sup>13</sup>R. Durscher and S. Roy, "Evaluation of thrust measurement techniques for dielectric barrier discharge actuators," *Exp. Fluids* **53**(4), 1165–1176 (2012).

<sup>14</sup>J. Clifton and T. Heaton, Potential advantages of a strong-motion velocity meter over a strong-motion accelerometer," *Seismol. Res. Lett.* **73**(3), 332–342 (2002).

<sup>15</sup>J. Bendat and A. Piersol, *Random Data Analysis and Measurement Procedures*, 4th ed. (Wiley, 2010), p. 331.

<sup>16</sup>J. Zito, R. Durscher, J. Soni, S. Roy, and D. Arnold, "Flow and force induction using micron size dielectric barrier discharge," *Appl. Phys. Lett.* **100**, 193502 (2012).

<sup>17</sup>J. Soni and S. Roy, "Low pressure characterization of DBD actuators," *Appl. Phys. Lett.* **102**, 112908 (2013).